

Impedance spectroscopy of chiral symmetric topoelectrical circuits


Selma Franca ^{1,2,*}, Torsten Seidemann ¹, Fabian Hassler,³ Jeroen van den Brink,^{1,4} and Ion Cosma Fulga¹

¹*Institute for Theoretical Solid State Physics, IFW Dresden and Würzburg-Dresden Cluster of Excellence ct.qmat, Helmholtzstr. 20, 01069 Dresden, Germany*

²*Université Grenoble Alpes, CNRS, Grenoble INP, Institut Néel, 38000 Grenoble, France*

³*JARA-Institute for Quantum Information, RWTH Aachen University, 52056 Aachen, Germany*

⁴*Institute for Theoretical Physics, TU Dresden, 01069 Dresden, Germany*

 (Received 29 September 2023; revised 24 April 2024; accepted 30 April 2024; published 5 June 2024)

Topoelectrical circuits are metamaterial realizations of topological features of condensed matter systems. In this work, we discuss experimental methods that allow a fast and straightforward detection of the spectral features of these systems from the two-point impedance of the circuit. This allows us to deduce the full spectrum of a topoelectrical circuit consisting of N sites from a single two-point measurement of the frequency-resolved impedance. In contrast, the standard methods rely on N^2 measurements of admittance matrix elements with a subsequent diagonalization on a computer. We experimentally test our approach by constructing a Fibonacci topoelectrical circuit. Although the spectrum of an infinite Fibonacci chain is fractal, i.e., more complex than the spectra of periodic systems, our approach is successful in recovering its eigenvalues. Our work promotes the topoelectrical circuits as an ideal platform to measure spectral properties of various (quasi)crystalline systems.

DOI: [10.1103/PhysRevB.109.L241103](https://doi.org/10.1103/PhysRevB.109.L241103)

Introduction. Theoretical studies of topological phases of matter often rely on toy models to elucidate physical mechanisms behind observed phenomena. Due to their underlying simplicity, toy models are challenging to realize in condensed matter settings prompting the need for metamaterials; classical or quantum systems designed to reproduce desired topological features of condensed matter systems. The initial proposal [1] involved photonic crystals where electromagnetic waves propagate unidirectionally along the boundary, thus forming the photonic analog of the integer quantum Hall effect (IQHE) [2]. In addition to photonic metamaterials [3–10], there are acoustic [11–18], mechanical [19–21], microwave [22–27], and electrical circuit [28–44] realizations of various topological phases.

Topoelectrical circuits are networks of nodes connected by electronic components such as resistors, capacitors, and inductors. They are described by an admittance matrix $Y(f)$ that represents the current response to a set $\mathbf{V}(f)$ of locally applied voltages at frequency f , and that is related to the circuit Laplacian that can be seen as an effective tight-binding Hamiltonian [30,36,45]. So far, the experimental characterization of these classical systems mostly relied on detecting topological boundary phenomena using two-point impedance measurements [30,45]. This impedance, $Z_{a,b}(f)$, can be determined by measuring the voltage response between the nodes a and b to an input current oscillating at a specific frequency. If this frequency corresponds to the energy of a topological boundary state of the circuit Laplacian, and if the nodes are chosen such that one is in the bulk of the system and the other in the region where this topological state is localized, the resulting two-point impedance is very large (divergent) in realistic (ideal)

systems. Thus, the presence of a topological boundary state (TBS) results in a single, isolated impedance peak. Moreover, the impedance between two corner nodes in finite electrical circuits was recently shown to exhibit size-dependent resonances and fractal features without a continuum analog once the electronic components between nodes have differing phase lags [46,47].

Gaining access to the full spectrum of the circuit Laplacian simulated by a topoelectrical circuit, beyond the detection of individual, spectrally isolated modes, is challenging. The spectra of topoelectrical circuits have so far been determined by measuring the full admittance matrix, element by element, and then diagonalizing it on a computer [48]. This is a time-consuming process, since the number of measurements scales quadratically (N^2) with the number of sites N in the system. Such disadvantageous scaling hinders the full spectrum measurement of a topoelectrical circuit, and undermines interest in realizing systems with intriguing spectral properties, like quasicrystals.

Quasicrystals are systems with incommensurate energy scales [49,50], whose spectra may be fractal, resulting in local power law singularities of the associated density of states [51]. Since they are much rarer in nature, their metamaterial realizations are even more relevant for studying their spectral properties [51,52]. The prototypical example in one-dimension is the Fibonacci chain, an array of sites related by two possible hopping strengths arranged into a quasiperiodic pattern [51]. Beyond having a fractal spectrum in the thermodynamic limit, this chain is interesting because it can be adiabatically related to a two-dimensional Hofstadter model that realizes the IQHE physics. Consequently, the Fibonacci chain can support TBSs [53,54].

In this work, we discuss how an extensive number of topoelectrical circuit modes can be detected from the linear

*selma.franca@neel.cnrs.fr

response function of the circuit. We identify the eigenvalues of the circuit Laplacian [48,55,56] by determining the resonances of the frequency-dependent two-point impedance through appropriate signal processing techniques. We test our approach under realistic conditions by constructing a topoelectrical Fibonacci chain. Despite having a fractal spectrum in the thermodynamic limit that is more sophisticated than the spectrum of a periodic system, we correctly identify most of the Fibonacci chain eigenvalues in a single frequency-resolved measurement by utilizing the chiral symmetry of the Fibonacci Hamiltonian.

We start by introducing the Hamiltonian of the finite Fibonacci chain and showing how the linear response function is able to detect the eigenvalues of the corresponding circuit Laplacian. We proceed with the experimental setup and discuss the measured data and corresponding numerical tools used to recover the spectrum.

Topoelectrical Fibonacci chain. In this work, we realize the 8th approximant of the infinite quasiperiodic Fibonacci chain consisting of $N = 34$ sites [51]. The Hamiltonian reads

$$H(\phi) = \sum_{n=1}^N t_n(\phi) c_{n+1}^\dagger c_n + \text{H.c.}, \quad (1)$$

where c_n^\dagger (c_n) represent the creation (annihilation) operator of a particle at site n . The hoppings $t_n(\phi) = \alpha + \beta \text{sign}[\chi_n(\phi)]$ ($\alpha, \beta \in \mathbb{R}$) alternate between two values t_A and t_B as a function of the index n , such that $\alpha = (t_A + t_B)/2$ and $\beta = (t_A - t_B)/2$. The alternation pattern is determined by the characteristic function $\chi_n(\phi) = \cos(\frac{2\pi n}{\tau} + \phi) - \cos(\frac{\pi}{\tau})$ with the golden ratio $\tau = \frac{1+\sqrt{5}}{2}$ and the phason angle $\phi \in [0, 2\pi)$ [53]. Setting $\phi = \pi$ creates the Fibonacci chain with two pairs of TBSs that belong to different topological gaps. These pairs of TBSs occur at opposite energies because the Hamiltonian obeys the chiral symmetry constraint $\mathcal{C}H(\phi)\mathcal{C}^\dagger = -H(\phi)$ with $C_{nm} = \delta_{nm}(-1)^n$. Besides being symmetric with respect to zero energy, the spectrum of an infinitely long Fibonacci chain is fractal [57]. The eigenvalues are arranged in a self-similar pattern, as we can divide the spectrum into three clusters (or bands) of eigenvalues, and each cluster can be further split into three subclusters, and so on [51].

In the following, we describe an electrical circuit that realizes the finite Fibonacci chain. In the Supplemental Material (SM) [58], we consider the system under periodic boundary conditions. The Fibonacci circuit consists of $N = 34$ nodes related by capacitors of distinct capacitances C_A and C_B that emulate the hoppings t_A and t_B of the tight-binding model. We show the circuit diagram inside the bulk of the system and the corresponding segment of a constructed circuit board in Figs. 1(a) and 1(b), respectively. The orange and green boxes in Fig. 1(a) represent two possible local environments of bulk circuit nodes that differ by whether identical capacitances (C_A, C_A) or distinct ones ($C_{A(B)}, C_{B(A)}$) are used to relate a node n to its neighbors. In the former (latter) case, for the grounding of node n we use a capacitor of capacitance $\tilde{C}_n = C_B$ ($\tilde{C}_n = C_A$) that is connected in parallel to an inductor of inductance L , such that the relation $\tilde{C}_n + C_{n-1} + C_n = 2C_A + C_B$ holds.

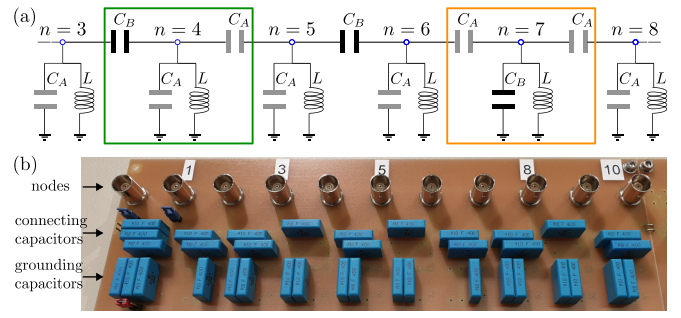


FIG. 1. Fibonacci topoelectrical circuit. (a) The circuit diagram between nodes $n = 3$ and $n = 8$. Orange and green boxes indicate two different configurations of topoelectrical circuit junctions. (b) A photograph of the corresponding segment of the circuit board. We see all elements of the circuit diagram of (a), except inductors that are located on the backside.

Each node is described by Kirchoff's law [30] $I_n = G_{n-1}(V_n - V_{n-1}) + G_n(V_n - V_{n+1}) + g_n V_n$, where $G_n = 2\pi j f C_n$ is the admittance between nodes n and $n + 1$, f is the frequency, $C_n \in \{C_A, C_B\}$ depending on $\text{sign}[\chi_n(\pi)]$, and $j^2 = -1$. The admittance g_n between node n and the ground equals $g_n = 2\pi j f \tilde{C}_n + 1/(2\pi j f L)$ with $\tilde{C}_n \in \{C_A, C_B\}$. By grouping all currents and voltages into vectors \mathbf{I} and \mathbf{V} , we obtain the admittance matrix $Y(f)$

$$Y(f) = \tilde{g}(f)\mathbb{I} - 2\pi j f \mathcal{L} \quad (2)$$

in terms of which Kirchoff's rules are given by $\mathbf{I}(f) = Y(f)\mathbf{V}(f)$. Here, $\tilde{g}(f) = 2\pi j f (2C_A + C_B) + 1/(2\pi j f L)$ and \mathcal{L} is the circuit Laplacian matrix with capacitances C_n in positions of hoppings t_n of the Fibonacci Hamiltonian Eq. (1).

To experimentally characterize the spectral properties of this circuit, we measure its response to the applied current $I(f)$. The voltage at node b is related to an input current at node a via the two-point impedance

$$Z_{a,b}(f) = \frac{V_a(f) - V_b(f)}{I_a(f)} = \sum_{k=1}^N \frac{|v_{k,a} - v_{k,b}|^2}{Y_k}, \quad (3)$$

that can be calculated from the eigenvalues $Y_k(f)$ and eigenvectors $v_k(f)$ of the admittance matrix [30].

Next, we describe how $Z_{a,b}(f)$ can be used to reconstruct the Fibonacci chain spectrum. From Eq. (3), we see that $Z_{a,b}(f)$ has a pole at frequency f_k every time $Y_k(f_k) = 0$. Since Eq. (2) relates the admittance matrix eigenvalues $Y_k = \tilde{g}(f) - 2\pi j f E_k$ with the circuit Laplacian eigenvalues E_k , setting $Y_k(f_k) = 0$ yields

$$E_k = 2C_A + C_B - \frac{1}{4\pi^2 L f_k^2}; \quad (4)$$

we note in passing, that the energies are measured in units of capacitance. Therefore, reconstructing E_k relies on identifying the resonance frequencies f_k of the response function $Z_{a,b}(f)$. In the following, we describe how this can be done in practice.

Experimental setup and measurement analysis. For our experimental realization, we have used capacitors with nominal values of capacitances $C_A = 50$ nF and $C_B = 100$ nF, and inductors with nominal inductances $L = 10$ μ H that were pre-selected to vary less than 2% from the corresponding nominal

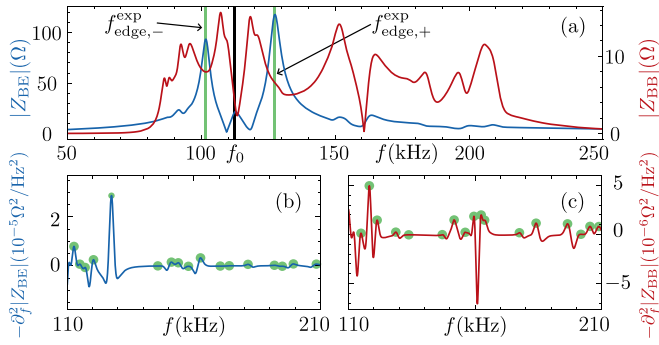


FIG. 2. Absolute values of the measured impedances $|Z_{BE}|$ and $|Z_{BB}|$ (a) and their second derivatives $-\partial_f^2|Z_{BE}|$ and $-\partial_f^2|Z_{BB}|$ (b) and (c) as a function of frequency f . The green circles indicate the peaks of $-\partial_f^2|Z_{BE}|$ and $-\partial_f^2|Z_{BB}|$ in the frequency range $(f_0, 250 \text{ kHz})$, with $f_0 = 112.5 \text{ kHz}$.

values of conductances and inductances. Importantly, these circuit elements have small but nonvanishing direct current resistances $R_C^{\text{dc}} \approx 25 \text{ m}\Omega$ and $R_L^{\text{dc}} \approx 85 \text{ m}\Omega$. In case of the inductors the resistance is frequency-dependent and goes from $R_L^{\text{ac}} \approx 105 \text{ m}\Omega$ (at 50 kHz) to $R_L^{\text{ac}} \approx 308 \text{ m}\Omega$ (at 250 kHz). For more details, see the SM [58].

All measurements were performed with the lock-in amplifier SR865A manufactured by Stanford Research Systems [58]. We consider two configurations for the voltage probes; the “bulk-edge” (BE) configuration is realized by placing probes at nodes $a = 1$ and $b = 15$, while the “bulk-bulk” (BB) configuration has the probes at nodes $a = 10$ and $b = 24$, see the SM [58]. According to Eq. (3), the positions of the voltage probes determine the weights of the corresponding eigenstates in the impedance response. This results in a very different frequency dependence of the response functions $|Z_{BE}|$ and $|Z_{BB}|$ in range $f \in (50 \text{ kHz}, 250 \text{ kHz})$, see Fig. 2(a). To analyze these results, it is useful to define the frequency $f_0 = 112.5 \text{ kHz}$ corresponding to $E = 0$ as determined from Eq. (4) and using experimental values for C_A , C_B and L .

Our first observation is that $|Z_{BE}|$ and $|Z_{BB}|$ have less features for frequencies $f < f_0$ corresponding to negative energies than for frequencies $f > f_0$ representing the positive part of the spectrum. This is a consequence of the nonlinear relationship between the eigenvalues E_k and resonant frequencies f_k in Eq. (4), that positions the resonant frequencies of the negative (positive) eigenvalues closer together (further apart). When this effect is combined with nonzero resistances R_C^{dc} , R_L^{dc} , and R_L^{ac} that broaden the delta peaks of the ideal response function into Lorentzians, the resonant peaks for frequencies $f < f_0$ are expected to be less visible than the ones for $f > f_0$ [58]. The second important feature of Fig. 2(a) is the observation that $|Z_{BE}|$ has two very prominent peaks at frequencies (indicated by green lines) for which $|Z_{BB}|$ does not show any prominent features. This suggests that these peaks are induced by TBSs [30]. From the corresponding frequencies $f_{\text{edge},-}^{\text{exp}} \approx 101.7 \text{ kHz}$ and $f_{\text{edge},+}^{\text{exp}} \approx 127.5 \text{ kHz}$ using Eq. (4), we obtain the energies $E_{\text{edge},-}^{\text{exp}} = -44.9 \text{ nF}$ and $E_{\text{edge},+}^{\text{exp}} = 44.2 \text{ nF}$. Note that the theoretical value for energy of the TBSs is $E_{\text{edge},\pm} = \pm 43.7 \text{ nF}$; the relative errors are $\delta^r = |(E_{\text{edge},-}^{\text{exp}} - E_{\text{edge},-})/E_{\text{edge},-}| = 2.75\%$

and $\delta^r = 1.14\%$, respectively. Importantly, having $|E_{\text{edge},-}^{\text{exp}}| \approx |E_{\text{edge},+}^{\text{exp}}| \approx |E_{\text{edge},\pm}|$ is the experimental confirmation that the realized topoelectrical circuit is chiral symmetric.

To determine more eigenvalues, we focus on the second derivative of the response function because differentiation reduces the amplitude of broader peaks in the $Z_{a,b}(f)$ signal, thus improving the detection of resonances that have been previously obscured by a broader but stronger background [59]. In practice, calculating this derivative from the original data set is challenging because measurements always include some noise that manifests as random high-frequency and small amplitude deviations from the ideal signal. Since noise becomes more prominent with differentiation, we eliminate it from original data using a low-pass, fourth-order Butterworth filter [60]. This filter has a maximally flat frequency response in the passband, thus not giving rise to any additional frequency dependence upon its application [60].

We employ two different strategies for extracting the Fibonacci chain spectrum. Our first approach is based on searching for the frequencies f_k^{exp} at which the function $-\partial_f^2|Z_{a,b}|$ (and consequently $|Z_{a,b}(f)|$) has peaks. To calculate $-\partial_f^2|Z_{a,b}|$, we employ the Butterworth filter with the cutoff frequency $f_c = 0.01 f_{\text{Nq}}$ on $|Z_{a,b}(f)|$; here, f_{Nq} denotes the Nyquist frequency defined as half of the sampling frequency f . Due to aforementioned grouping effect of individual peaks for frequencies $f < f_0$, looking for 34 most prominent peaks of $-\partial_f^2|Z_{a,b}|$ in the entire frequency range does not produce satisfying results. Because of the chiral symmetry, we can instead focus on the frequency range $(f_0, 250 \text{ kHz})$ that corresponds to the positive part of the spectrum consisting of 17 eigenvalues. Using the SCIPY Python library [61], we find all the peaks of $-\partial_f^2|Z_{BE}|$ and $-\partial_f^2|Z_{BB}|$ in this frequency range and choose the 17 most prominent ones for both curves. These peaks are indicated with green circles in Figs. 2(b) and 2(c) for $-\partial_f^2|Z_{BE}|$ and $-\partial_f^2|Z_{BB}|$, respectively.

The corresponding spectra are constructed from pairs $(-E_k^{\text{exp}}, E_k^{\text{exp}})$, with E_k^{exp} obtained from f_k^{exp} using Eq. (4). We plot these spectra in Figs. 3(a) and 3(b) for the BE and BB voltage probe configurations, respectively, along with the theoretical eigenvalues E_k . We observe that both voltage probes are successful in detecting the edges of the upper band (and consequently the lower band), along with its inner subbands. The BE probe captures accurately the energies of two pairs of TBSs but it detects a single resonance per pair. This behavior is also present for an ideal circuit, and originates from the energy degeneracy of two TBSs. On the other side, the BB probe detects two resonances inside the topological gap but is less accurate in measuring the energies of TBSs. In total, for the BE probe the mean absolute error $\delta^{\text{avg}} = \sum_{k=1}^N |E_k - E_k^{\text{exp}}|/N$ equals $\delta_{\text{BE}}^{\text{avg}} = 4.87 \text{ nF}$ while the median error is $\delta_{\text{BE}}^m = 3.81 \text{ nF}$. For the BB probe, we find $\delta_{\text{BB}}^{\text{avg}} = 4.17 \text{ nF}$ and $\delta_{\text{BB}}^m = 3.18 \text{ nF}$.

As these errors are small compared to the total energy range, we conclude that searching for peaks of $-\partial_f^2|Z_{a,b}|$ is a fruitful strategy to recover the full spectrum. However, this approach takes into account only the amplitude of the frequency-dependent response function thus missing possible information hidden in its phase component. We rectify this with our second approach that is based on fitting the full

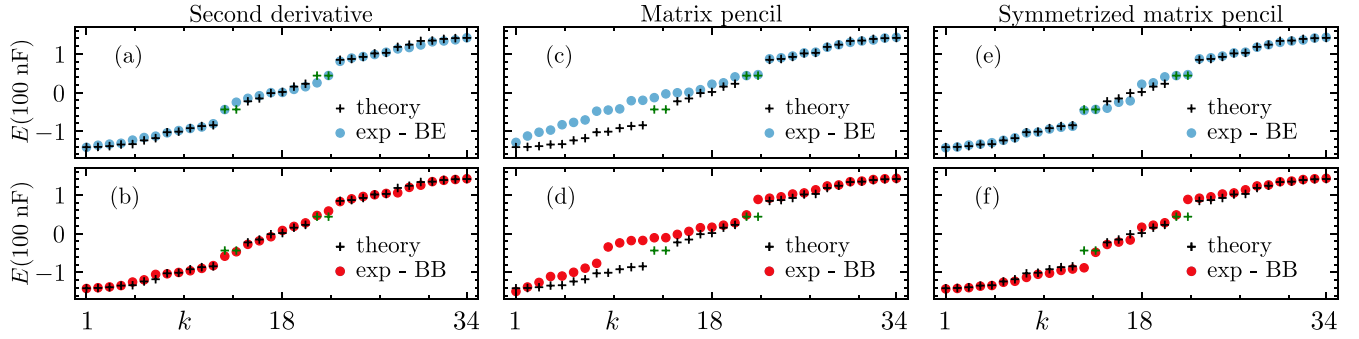


FIG. 3. Comparison between the theoretical and experimental spectra obtained using different methods of recovery. Here, the green crosses indicate TBSs. The eigenvalues in (a) and (b) are given by the maxima of $-\partial_f^2|Z_{BE}|$ and $-\partial_f^2|Z_{BB}|$, respectively. (c) and (d) show 34 resonant frequencies detected with the MP method. (e) and (f) are obtained by mirroring the 17 largest positive eigenvalues from (c) and (d) with respect to $E = 0$.

signal $-\partial_f^2 Z_{a,b}$ to the linear combination of Lorentzians. To eliminate noise from the data, we use the Butterworth filter separately on $\Re[Z_{a,b}(f)]$ and $\Im[Z_{a,b}(f)]$ before determining $\partial_f^2 Z_{a,b} = \partial_f^2 \Re[Z_{a,b}] + j \partial_f^2 \Im[Z_{a,b}]$. We use frequency cutoffs $f_c = 0.03 f_{Nq}$ ($f_c = 0.01 f_{Nq}$) for the BE (BB) configuration of voltage probes. The resulting signal $-\partial_f^2 Z_{a,b}$ is Fourier transformed into the time domain signal $Z_{a,b}^{(2)}(t) = \mathcal{F}[-\partial_f^2 Z_{a,b}]$ that is fitted to a sum of N damped exponentials as $Z_{a,b}^{(2)}(t) = \sum_{k=1}^N A_k^{\text{exp}} e^{j\phi_k^{\text{exp}}} e^{(\alpha_k^{\text{exp}} + 2\pi j f_k^{\text{exp}})t}$, where A_k^{exp} , ϕ_k^{exp} , α_k^{exp} and f_k^{exp} are the amplitudes, phases, damping factors and frequencies of the sinusoids, respectively. Assuming $t = mT$ where $m = 0, \dots, N-1$ and T is the sampling period, the exponential factor becomes $e^{(\alpha_k^{\text{exp}} + 2\pi j f_k^{\text{exp}})mT} = z_k^m$, where $z_k = e^{(\alpha_k^{\text{exp}} + 2\pi j f_k^{\text{exp}})T}$. The poles z_k are found by solving a generalized eigenvalue equation using a matrix pencil (MP) operator that is constructed from the values $Z_{a,b}^{(2)}(t)$ [62–64], see also the SM [58]. With 34 eigenvalues in theory, we look for 34 poles in our calculation.

The resulting spectrum, obtained using Eq. (4), is shown in Figs. 3(c) and 3(d) for both voltage probe configurations. While this approach can reconstruct the entire spectrum, we see that for both configurations it works better for positive eigenvalues. In general, the accuracy of the MP method declines with energy due to the aforementioned grouping effect of resonances, resulting in 15 (19) poles corresponding to negative (positive) energies for both probes. The additional positive poles arise at $E \sim 1$ nF that is very close to $E = 0$ in comparison with the energy scale of the chain. In the case of the BE probe where the TBSs dominate the response of the circuit, the MP method overestimates their number in the upper topological gap but captures their energies well. For the BB probe, the method finds a single TBS with $E > 0$ and attributes the missing TBS resonance to the upper band. In total, we find $\delta_{BE}^{\text{avg}} = 21.67$ nF, $\delta_{BE}^m = 14.09$ nF, and $\delta_{BB}^{\text{avg}} = 19.83$ nF, $\delta_{BB}^m = 11.54$ nF. Such large values of errors reflect the fact that the MP method misses to capture the negative eigenvalues accurately.

The results of the MP method can be improved by utilizing the chiral symmetry constraint, i.e., by constructing spectra from pairs $(-E_k^{\text{exp}}, E_k^{\text{exp}})$, where $E_k^{\text{exp}} > 0$ are 17 largest positive eigenvalues from Figs. 3(c) and 3(d). Results are shown in Figs. 3(e) and 3(f) for BE and BB configurations, respectively.

This combined approach reduces the errors of measurements to $\delta_{BE}^{\text{avg}} = 4.24$ nF, $\delta_{BE}^m = 2.22$ nF for the BE probe and $\delta_{BB}^{\text{avg}} = 7.68$ nF, $\delta_{BB}^m = 5.22$ nF for the BB probe. Therefore, combining the MP method with the chiral symmetry constraint works the best for the BE probe, while searching for the peaks of $-\partial_f^2|Z_{a,b}|$ yields better results for the BB probe.

For both probes, our best results have $\delta_{a,b}^{\text{avg}} \approx \delta_E/2$, where $\delta_E = 8.55$ nF is a theoretical average energy spacing. These results could be improved by reducing the noise of the measurement and the resistances of circuit elements. Contrary to the present study that separately measured $V_a(f)$, $V_b(f)$, $I_a(f)$, employing additional lock-in amplifiers would allow for a simultaneous measurement of all three quantities thus reducing the noise. Reducing resistances of circuit elements, on the other hand, is not straightforward: e.g., lowering R_L^{ac} (100 kHz) generally assumes reducing the inductance L of inductors, thus increasing the frequency range of the spectrum and correspondingly $R_L^{\text{ac}}(f)$. Consequently, the inductors produce additional heating that washes out features due to the increased noise. An interesting idea for future research is to investigate whether superconducting elements with significantly smaller resistances can improve the accuracy of our results.

Conclusion. In this work, we have shown how the response function of an electrical circuit can be used to recover the full spectrum of an underlying chiral symmetric condensed matter system. We have constructed a Fibonacci topoelectrical chain that has a fractal spectrum in the thermodynamic limit due to its quasicrystalline nature. Using the chiral symmetry constraint of the spectrum, we have demonstrated that it can be recovered from a single measurement using two distinct methods of data analysis. We have corroborated our findings by changing the positions of the voltage probes and boundary conditions (open, periodic) of the Fibonacci topoelectrical circuit [58]. In conclusion, our work promotes topoelectrical circuits as an ideal metamaterial platform for studying spectral properties of (quasi)crystalline systems.

Acknowledgments. We thank U. Nitzsche for technical assistance. This work was supported by the Deutsche Forschungsgemeinschaft (DFG, German Research Foundation) under Germany's Excellence Strategy through the Würzburg-Dresden Cluster of Excellence on Complexity and

Topology in Quantum Matter–ct.qmat(EXC 2147, Project-Id No. 390858490) and under Germany’s Excellence Strategy–Cluster of Excellence Matter and Light for Quantum Computing (ML4Q) EXC 2004/1–390534769. S.F. acknowledges

financial support from the European Union Horizon 2020 research and innovation program under Grant Agreement No. 829044 (SCHINES).

The authors declare no competing interests.

- [1] F. D. M. Haldane and S. Raghu, Possible realization of directional optical waveguides in photonic crystals with broken time-reversal symmetry, *Phys. Rev. Lett.* **100**, 013904 (2008).
- [2] K. V. Klitzing, G. Dorda, and M. Pepper, New method for high-accuracy determination of the fine-structure constant based on quantized Hall resistance, *Phys. Rev. Lett.* **45**, 494 (1980).
- [3] L. Lu, J. D. Joannopoulos, and M. Soljačić, Topological photonics, *Nat. Photon* **8**, 821 (2014).
- [4] J. M. Zeuner, M. C. Rechtsman, Y. Plotnik, Y. Lumer, S. Nolte, M. S. Rudner, M. Segev, and A. Szameit, Observation of a topological transition in the bulk of a non-Hermitian system, *Phys. Rev. Lett.* **115**, 040402 (2015).
- [5] S. Weimann, M. Kremer, Y. Plotnik, Y. Lumer, S. Nolte, K. G. Makris, M. Segev, M. C. Rechtsman, and A. Szameit, Topologically protected bound states in photonic parity-time-symmetric crystals, *Nat. Mater.* **16**, 433 (2017).
- [6] J. Noh, W. A. Benalcazar, S. Huang, M. J. Collins, K. P. Chen, T. L. Hughes, and M. C. Rechtsman, Topological protection of photonic mid-gap defect modes, *Nat. Photon.* **12**, 408 (2018).
- [7] E. Saei Ghareh Naz, I. C. Fulga, L. Ma, O. G. Schmidt, and J. van den Brink, Topological phase transition in a stretchable photonic crystal, *Phys. Rev. A* **98**, 033830 (2018).
- [8] X.-D. Chen, W.-M. Deng, F.-L. Shi, F.-L. Zhao, M. Chen, and J.-W. Dong, Direct observation of corner states in second-order topological photonic crystal slabs, *Phys. Rev. Lett.* **122**, 233902 (2019).
- [9] S. Mittal, V. V. Orre, G. Zhu, M. A. Gorlach, A. Poddubny, and M. Hafezi, Photonic quadrupole topological phases, *Nat. Photon.* **13**, 692 (2019).
- [10] A. El Hassan, F. K. Kunst, A. Moritz, G. Andler, E. J. Bergholtz, and M. Bourennane, Corner states of light in photonic waveguides, *Nat. Photon.* **13**, 697 (2019).
- [11] D. Torrent and J. Sánchez-Dehesa, Acoustic analogue of graphene: Observation of Dirac cones in acoustic surface waves, *Phys. Rev. Lett.* **108**, 174301 (2012).
- [12] Z. Yang, F. Gao, X. Shi, X. Lin, Z. Gao, Y. Chong, and B. Zhang, Topological acoustics, *Phys. Rev. Lett.* **114**, 114301 (2015).
- [13] L. Fan, W.W. Yu, S.Y. Zhang, H. Zhang, and J. Ding, Zak phases and band properties in acoustic metamaterials with negative modulus or negative density, *Phys. Rev. B* **94**, 174307 (2016).
- [14] H. Xue, Y. Yang, F. Gao, Y. Chong, and B. Zhang, Acoustic higher-order topological insulator on a kagome lattice, *Nat. Mater.* **18**, 108 (2019).
- [15] X. Ni, M. Weiner, A. Alù, and A. B. Khanikaev, Observation of higher-order topological acoustic states protected by generalized chiral symmetry, *Nat. Mater.* **18**, 113 (2019).
- [16] D. J. Apigo, W. Cheng, K. F. Dobiszewski, E. Prodan, and C. Prodan, Observation of topological edge modes in a quasiperiodic acoustic waveguide, *Phys. Rev. Lett.* **122**, 095501 (2019).
- [17] X. Ni, K. Chen, M. Weiner, D. J. Apigo, C. Prodan, A. Alù, E. Prodan, and A. B. Khanikaev, Observation of Hofstadter butterfly and topological edge states in reconfigurable quasiperiodic acoustic crystals, *Commun. Phys.* **2**, 55 (2019).
- [18] Z.-G. Chen, W. Tang, R.-Y. Zhang, Z. Chen, and G. Ma, Landau-Zener transition in the dynamic transfer of acoustic topological states, *Phys. Rev. Lett.* **126**, 054301 (2021).
- [19] R. Süsstrunk and S. D. Huber, Observation of phononic helical edge states in a mechanical topological insulator, *Science* **349**, 47 (2015).
- [20] K. Bertoldi, V. Vitelli, J. Christensen, and M. van Hecke, Flexible mechanical metamaterials, *Nat. Rev. Mater.* **2**, 17066 (2017).
- [21] M. Serra-Garcia, V. Peri, R. Süsstrunk, O. R. Bilal, T. Larsen, L. G. Villanueva, and S. D. Huber, Observation of a phononic quadrupole topological insulator, *Nature (London)* **555**, 342 (2018).
- [22] M. Bellec, U. Kuhl, G. Montambaux, and F. Mortessagne, Topological transition of Dirac points in a microwave experiment, *Phys. Rev. Lett.* **110**, 033902 (2013).
- [23] W. Hu, J. C. Pillay, K. Wu, M. Pasek, P. P. Shum, and Y. D. Chong, Measurement of a topological edge invariant in a microwave network, *Phys. Rev. X* **5**, 011012 (2015).
- [24] B. M. Anderson, R. Ma, C. Owens, D. I. Schuster, and J. Simon, Engineering topological many-body materials in microwave cavity arrays, *Phys. Rev. X* **6**, 041043 (2016).
- [25] C. W. Peterson, W. A. Benalcazar, T. L. Hughes, and G. Bahl, A quantized microwave quadrupole insulator with topologically protected corner states, *Nature (London)* **555**, 346 (2018).
- [26] Y. Yu, W. Song, C. Chen, T. Chen, H. Ye, X. Shen, Q. Cheng, and T. Li, Phase transition of non-Hermitian topological edge states in microwave regime, *Appl. Phys. Lett.* **116**, 211104 (2020).
- [27] S. Ma and S. M. Anlage, Microwave applications of photonic topological insulators, *Appl. Phys. Lett.* **116**, 250502 (2020).
- [28] J. Ningyuan, C. Owens, A. Sommer, D. Schuster, and J. Simon, Time- and site-resolved dynamics in a topological circuit, *Phys. Rev. X* **5**, 021031 (2015).
- [29] V. V. Albert, L. I. Glazman, and L. Jiang, Topological properties of linear circuit lattices, *Phys. Rev. Lett.* **114**, 173902 (2015).
- [30] C. H. Lee, S. Imhof, C. Berger, F. Bayer, J. Brehm, L. W. Molenkamp, T. Kiessling, and R. Thomale, Topoelectrical circuits, *Commun. Phys.* **1**, 39 (2018).
- [31] T. Goren, K. Plekhanov, F. Appas, and K. Le Hur, Topological Zak phase in strongly coupled LC circuits, *Phys. Rev. B* **97**, 041106(R) (2018).
- [32] Y. Li, Y. Sun, W. Zhu, Z. Guo, J. Jiang, T. Kariyado, H. Chen, and X. Hu, Topological LC-circuits based on microstrips and observation of electromagnetic modes with orbital angular momentum, *Nat. Commun.* **9**, 4598 (2018).
- [33] T. Hofmann, T. Helbig, C. H. Lee, M. Greiter, and R. Thomale, Chiral voltage propagation and calibration in a topoelectrical Chern circuit, *Phys. Rev. Lett.* **122**, 247702 (2019).

- [34] R. Haenel, T. Branch, and M. Franz, Chern insulators for electromagnetic waves in electrical circuit networks, *Phys. Rev. B* **99**, 235110 (2019).
- [35] W. Zhu, Y. Long, H. Chen, and J. Ren, Quantum valley Hall effects and spin-valley locking in topological Kane-Mele circuit networks, *Phys. Rev. B* **99**, 115410 (2019).
- [36] T. Helbig, T. Hofmann, S. Imhof, M. Abdelghany, T. Kiessling, L. W. Molenkamp, C. H. Lee, A. Szameit, M. Greiter, and R. Thomale, Generalized bulk-boundary correspondence in non-Hermitian topoelectrical circuits, *Nat. Phys.* **16**, 747 (2020).
- [37] T. Hofmann, T. Helbig, F. Schindler, N. Salgo, M. Brzezińska, M. Greiter, T. Kiessling, D. Wolf, A. Vollhardt, A. Kabaši, C. H. Lee, A. Bilušić, R. Thomale, and T. Neupert, Reciprocal skin effect and its realization in a topoelectrical circuit, *Phys. Rev. Res.* **2**, 023265 (2020).
- [38] Y. Wang, H. M. Price, B. Zhang, and Y. D. Chong, Circuit implementation of a four-dimensional topological insulator, *Nat. Commun.* **11**, 2356 (2020).
- [39] S. M. Rafi-Ul-Islam, Z. Bin Siu, and M. B. A. Jalil, Topoelectrical circuit realization of a Weyl semimetal heterojunction, *Commun. Phys.* **3**, 72 (2020).
- [40] J. Dong, V. Juričić, and B. Roy, Topoelectric circuits: Theory and construction, *Phys. Rev. Res.* **3**, 023056 (2021).
- [41] T. Kotwal, F. Moseley, A. Stegmaier, S. Imhof, H. Brand, T. Kießling, R. Thomale, H. Ronellenfitsch, and J. Dunkel, Active topoelectrical circuits, *Proc. Natl. Acad. Sci. USA* **118**, e2106411118 (2021).
- [42] H. Yang, L. Song, Y. Cao, and P. Yan, Realization of Wilson fermions in topoelectrical circuits, *Commun. Phys.* **6**, 211 (2023).
- [43] X. Zheng, T. Chen, and X. Zhang, Topoelectrical circuit realization of quadrupolar surface semimetals, *Phys. Rev. B* **106**, 035308 (2022).
- [44] H. Zhang, T. Chen, L. Li, C. H. Lee, and X. Zhang, Electrical circuit realization of topological switching for the non-Hermitian skin effect, *Phys. Rev. B* **107**, 085426 (2023).
- [45] S. Imhof, C. Berger, F. Bayer, J. Brehm, L. W. Molenkamp, T. Kiessling, F. Schindler, C. H. Lee, M. Greiter, T. Neupert, and R. Thomale, Topoelectrical-circuit realization of topological corner modes, *Nat. Phys.* **14**, 925 (2018).
- [46] H. Sahin, Z. B. Siu, S. M. Rafi-Ul-Islam, J. F. Kong, M. B. A. Jalil, and C. H. Lee, Impedance responses and size-dependent resonances in topoelectrical circuits via the method of images, *Phys. Rev. B* **107**, 245114 (2023).
- [47] X. Zhang, B. Zhang, H. Sahin, Z. B. Siu, S. M. Rafi-Ul-Islam, J. F. Kong, B. Shen, M. B. A. Jalil, R. Thomale, and C. H. Lee, Anomalous fractal scaling in two-dimensional electric networks, *Commun. Phys.* **6**, 151 (2023).
- [48] A. Stegmaier, S. Imhof, T. Helbig, T. Hofmann, C. H. Lee, M. Kremer, A. Fritzsche, T. Feichtner, S. Klembt, S. Höfling, I. Boettcher, I. C. Fulga, L. Ma, O. G. Schmidt, M. Greiter, T. Kiessling, A. Szameit, and R. Thomale, Topological defect engineering and \mathcal{PT} symmetry in non-Hermitian electrical circuits, *Phys. Rev. Lett.* **126**, 215302 (2021).
- [49] D. Lenz and P. Stollmann, Aperiodic order and quasicrystals: Spectral properties, *Ann. Henri Poincaré* **4**, 933 (2003).
- [50] A. S. Pikovsky, M. A. Zaks, U. Feudel, and J. Kurths, Singular continuous spectra in dissipative dynamics, *Phys. Rev. E* **52**, 285 (1995).
- [51] A. Jagannathan, The Fibonacci quasicrystal: Case study of hidden dimensions and multifractality, *Rev. Mod. Phys.* **93**, 045001 (2021).
- [52] D. Tanese, E. Gurevich, F. Baboux, T. Jacqmin, A. Lemaître, E. Galopin, I. Sagnes, A. Amo, J. Bloch, and E. Akkermans, Fractal energy spectrum of a polariton gas in a Fibonacci quasiperiodic potential, *Phys. Rev. Lett.* **112**, 146404 (2014).
- [53] Y. E. Kraus, Y. Lahini, Z. Ringel, M. Verbin, and O. Zilberberg, Topological states and adiabatic pumping in quasicrystals, *Phys. Rev. Lett.* **109**, 106402 (2012).
- [54] M. Verbin, O. Zilberberg, Y. E. Kraus, Y. Lahini, and Y. Silberberg, Observation of topological phase transitions in photonic quasicrystals, *Phys. Rev. Lett.* **110**, 076403 (2013).
- [55] A. Stegmaier, H. Brand, S. Imhof, A. Fritzsche, T. Helbig, T. Hofmann, I. Boettcher, M. Greiter, C. H. Lee, G. Bahl, A. Szameit, T. Kießling, R. Thomale, and L. K. Upreti, Realizing efficient topological temporal pumping in electrical circuits, *Phys. Rev. Res.* **6**, 023010 (2024).
- [56] D. Zou, T. Chen, H. Meng, Y. S. Ang, X. Zhang, and C. H. Lee, Experimental observation of exceptional bound states in a classical circuit network, [arXiv:2308.01970](https://arxiv.org/abs/2308.01970).
- [57] A. Sütő, Singular continuous spectrum on a Cantor set of zero Lebesgue measure for the Fibonacci Hamiltonian, *J. Stat. Phys.* **56**, 525 (1989).
- [58] See Supplemental Material at <http://link.aps.org/supplemental/10.1103/PhysRevB.109.L241103> for details of the experimental realization before discussing how realistic capacitors and inductors affect the two point impedance. We proceed with a discussion on the matrix pencil method, and show reconstructed spectra for the system under periodic boundary conditions. Using the localization length of topological edge states, we determine the type of nodes (bulk, edge) inside the circuit. We then discuss how the choice of nodes at which we place our probes affect the measured impedance of the circuit, which also includes Refs. [30,45,61,62,65–68].
- [59] T. O’Haver, *A Pragmatic Introduction to Signal Processing 2023: With applications in scientific measurement*, McGraw-Hill Series in Electrical Engineering (Independently Published, 2023).
- [60] S. Butterworth, On the theory of filter amplifiers, *Experimental Wireless & the Wireless Engineer*, **7**, 536 (1930).
- [61] S. Franca, T. Seidemann, F. Hassler, J. van den Brink, and I. C. Fulga, Impedance spectroscopy of chiral symmetric topoelectrical circuits, Zenodo (2023), doi:10.5281/zenodo.8386622.
- [62] Y. Hua and T. Sarkar, Matrix pencil method for estimating parameters of exponentially damped/undamped sinusoids in noise, *IEEE Trans. Acoust. Speech Signal Process.* **38**, 814 (1990).
- [63] L. Vanhamme, T. Sundin, P. V. Hecke, and S. V. Huffel, MR spectroscopy quantitation: A review of time-domain methods, *NMR Biomed.* **14**, 233 (2001).
- [64] T. P. Zielinski and K. Duda, Frequency and damping estimation methods - an overview, *Metrology Measure. Syst.* **18**, 505 (2011).
- [65] W. Hayt and J. Buck, *Engineering Electromagnetics* (McGraw-Hill Higher Education, New York, 2006).
- [66] C. M. Hwee, Matrix Pencil method as a signal processing technique performance and application on power

- systems signals, Ph.D. thesis, National University of Singapore, 2013.
- [67] E. Assiimwe, E. Mwangi, and D. B. O. Konditi, A matrix pencil method for the efficient computation of direction of arrival estimation for weakly correlated signals using uniform linear array in a low SNR regime, *Int. J. Engineer. Technol.* **11**, 1347 (2018).
- [68] J. K. Asbóth, L. Oroszlány, and A. Pályi, *A Short Course on Topological Insulators* (Springer International Publishing, New York, 2016).